Author for correspondence:
Leif Karlstrom,
E-mail: leif@uoregon.edu

Fluid resonance in elastic-walled englacial transport networks

Maria McQuillan and Leif Karlstrom

Department of Earth Sciences, University of Oregon, Eugene, OR, USA

Abstract

Englacial water transport is an integral part of the glacial hydrologic system, yet the geometry of englacial structures remains largely unknown. In this study, we explore the excitation of fluid resonance by small amplitude waves as a probe of englacial geometry. We model a hydraulic network consisting of one or more tabular cracks that intersect a cylindrical conduit, subject to oscillatory wave motion initiated at the water surface. Resulting resonant frequencies and quality factors are diagnostic of fluid properties and geometry of the englacial system. For a single crack–conduit system, the fundamental mode involves gravity-driven fluid sloshing between the conduit and the crack, at frequencies between 0.02 and 10 Hz for typical glacial parameters. Higher frequency modes include dispersive Krauklis waves generated within the crack and tube waves in the conduit. But we find that crack lengths are often well constrained by fundamental mode frequency and damping rate alone for settings that include alpine glaciers and ice sheets. Branching crack geometry and dip, ice thickness and source excitation function help define limits of crack detectability for this mode. In general, we suggest that identification of eigenmodes associated with wave motion in time series data may provide a pathway toward inferring englacial hydrologic structures.

Introduction

The englacial hydrologic system controls water transport from the surface to the base of glaciers, regulating the sensitivity of glaciers and ice sheets to environmental influences. The geometry of water transport pathways is poorly understood, but it determines the efficacy of water transport to the glacier base (Fountain and others, 2005) and thus strongly affects subglacial drainage and ice flow dynamics (Schoof, 2010; Bartholomew and others, 2012; Banwell and others, 2016). In this study, we investigate how the detection of fluid resonance in subsurface cracks (quasi-planar cavities at interfaces or arising from fractures, with small opening compared to the other two dimensions) and conduits (long channels with roughly equant cross-sectional dimensions) may be used to interrogate hidden water transport pathways in glaciers and ice sheets.

The englacial system has been studied through various direct and indirect methods. Direct speleological observations (e.g. Vatne, 2001), in situ monitoring of boreholes with cameras (e.g. Fountain and others, 2005), as well as indirect imaging from various types of ice-penetrating radar (e.g. Catania and others, 2008; Badgeley and others, 2017), suggest that the englacial system can be composed of cracks, conduits or possibly both. However, these methods are limited in their scope and generally fail to inform water transport dynamics or internal geometry such as is predicted from theory (e.g. Röthlisberger, 1972; Shreve, 1972; Spring and Hutter, 1982; Gulley and others, 2009). Therefore, we look to other methods that may provide more insight.

Unsteady fluid motion has been used to probe the subglacial hydrologic system for decades. For example, slug tests and borehole studies have been conducted to infer basal structures (Stone and others, 1997; Kulessa and others, 2005), subglacial storage and subglacial drainage efficiency (Iken and others, 1996; Kulessa and others, 2005; Kavanaugh and others, 2010; Rada and Schoof, 2018). More recently, seismic and geodetic studies have used transients in internal and basal water pressures on hour to day timescales, to infer basal sliding and ice flow dynamics (Iken, 1972; Engelhardt and Kamb, 1997; Kavanaugh and Clarke, 2001; Kavanaugh and others, 2010; Andrews and others, 2018).

Oscillatory fluid motions, generally at much higher frequencies, have also been leveraged to infer subsurface transport structures. Fluid oscillations in a confining structure lead to resonance at distinct frequencies or 'eigenmodes' that can be related to excitation mechanisms and the geometry of a resonator. This phenomenon has seen application in oil and gas exploration and volcanology (Aki and others, 1977; Holzhausen and Egan, 1986; Chouet, 1988; Chen and others, 1996; Mondal, 2010; Liang and others, 2020), as well as some studies in the glacial environment (Lipovsky and Dunham, 2015; Roeoesli and others, 2016; Podolskiy, 2020). Here, we aim to advance this particular field of research, by investigating the limits to which fluid resonance can be used to define a variety of englacial geometries.

Because the problem of fluid resonance in elastic-walled transport structures has been studied in other contexts, we present a synthesis of relevant results and an overview of resonant modes using the englacial system to constrain parameters. Through this investigation we find one mode – a coupled oscillation between a conduit and branching crack – of particular
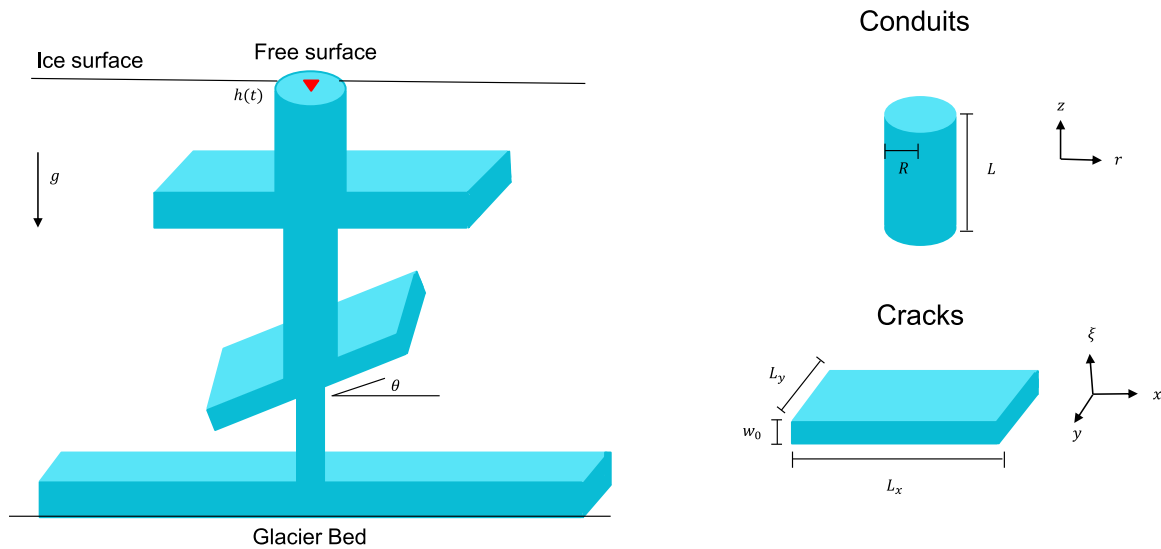
Fig. 1. Idealized model of the englacial system showing multiple cracks branching from a central conduit. Cracks are defined by two length scales L_x and L_y and opening w_0. Conduit sections are defined by a length L and a radius R. Cracks may also be dipping at an angle θ with respect to the conduit axis. The free surface is denoted by a red triangle. $h(t)$ is the height of the water surface in reference to an unperturbed fluid surface at atmospheric pressure.

interest, and dedicate much of the subsequent text to understanding this mode. In particular, we explore the limits to which the coupled mode provides information about the geometry of cracks branching from a central conduit connected to the surface, considering the influence of the flow regime within the conduit, crack dip and the excitation function that initiates wave motion. Finally, we apply our results to published high-frequency pressure time series data, and discuss the limits of subsurface crack detectability using fluid resonance in both alpine and ice-sheet environments.

Theory

We model the englacial system as a vertical tube with a circular cross section that may be connected to one or more dipping rectangular cracks, as seen in Fig. 1. Generalizations to conduits with variable radii, non-circular cross-sectional geometry or along-axis curvature are fairly straightforward extensions, but are not explored here. We assume that the fluid in the englacial system is pure water (no bubbles or sediment). Additionally, we neglect any energy dissipation from elastic waves emitted from the crack and tube walls and assume that the surrounding ice is homogeneous (e.g. Tsai and Rice, 2010). This last assumption is not strictly valid for cracks at the glacier bed between ice and till or bedrock, but we do not consider bi-material interfaces or inhomogeneous material properties here.

Governing equations: fluid-filled conduit

In the conduit, we solve the Navier–Stokes equations for flow of a viscous, compressible fluid in a pipe. We linearize around a static background state upon which small amplitude perturbations are superimposed at long wavelengths compared to crack openings and the conduit radius. Thus we can consider the fluid pressure to be uniform in the radial direction and fluid velocity to be axisymmetric and unidirectional. Finally, we assume a linearized equation of state for water in the conduit, giving rise to a constant fluid sound speed. The description and numerical implementation of equations in this section essentially follows Liang and others (2020), which is the modeling framework on which our study is built.

We use cross-sectionally averaged governing equations for fluid motion in a conduit with a constant radius R and length

L, which could apply to distinct conduit sections as depicted in Fig. 1. Cross-sectional averaging is defined by the operator $\langle\rangle$, acting on a generic function Φ of vertical position z, radial coordinate r and time t:

$$\langle\Phi(z, t)\rangle = \frac{2}{R^2}\int_0^R \Phi(z, r, t)r\,\mathrm{d}r. \tag{1}$$

We will generally omit explicit listing of function arguments except when necessary in what follows. Using this width-averaged description we solve the following governing equations in the conduit sections:

$$\frac{\partial\rho}{\partial t} + \rho_0\frac{\partial u_z}{\partial z} = 0, \tag{2}$$

$$\rho_0\frac{\partial u_z}{\partial t} + \frac{\partial p}{\partial z} = \langle\nabla\cdot\tau\rangle_z, \tag{3}$$

$$\frac{1}{\rho_0}\frac{\partial\rho}{\partial t} = \frac{1}{K_\mathrm{f}}\frac{\partial p}{\partial t} \tag{4}$$

where $u_z = \langle v_z\rangle$ is the cross-sectionally averaged vertical velocity, ρ is the fluid density with ρ_0 its constant and uniform background value, p is the fluid pressure, τ is the viscous stress tensor and K_f is the bulk modulus of water (numerical values for parameters are listed in Table 1). For our numerical experiments we assume fluid flow is fully developed, and the vertical component of the cross-sectionally averaged shear stress term becomes

$$\langle\nabla\cdot\tau\rangle_z = -\frac{8\mu}{R^2}u_z, \tag{5}$$

with μ as the dynamic viscosity of water. The limits for which this assumption is valid will be evaluated and discussed later for specific resonant modes.

To supplement the governing Eqns (2–4), we impose no slip boundary conditions at the conduit walls to ensure no fluid is transferred out or into the system. At the top of the conduit, the water surface is allowed to move freely, resulting in the

Table 1. Values for glacial parameters

Parameter symbol	Name	Value	Units
g	Gravitational acceleration	9.8	m s^{-2}
L	Conduit length	10–3000	m
R	Conduit radius	0.01–1	m
L_x	Crack length in x	1–3000	m
L_y	Crack length in y	1–3000	m
w_0	Unperturbed crack opening	1–200	mm
K_f	Fluid bulk modulus	1.98	GPa
ρ_0	Fluid density	1000	kg m^{-3}
μ	Dynamic viscosity	1.8×10^{-3}	Pa s
G	Shear modulus	3.5	GPa
ν	Poisson's ratio	0.31	–
κ	Crack storativity constant	0.4808	–
c_T	Tube wave speed	1125	m s^{-1}
c_0	Acoustic wave speed	1400	m s^{-1}

linearized boundary condition:

$$p|_{z=L} = \rho_0\, g h(t) + P_{\text{source}}(t), \qquad (6)$$

where g is the gravity, P_{source} is an externally imposed source function and $h(t)$ is the displacement of the fluid surface around hydrostatic equilibrium. $h(t)$ can be calculated using the cross-sectionally averaged fluid velocity at the surface:

$$u_z|_{z=L} = \frac{\mathrm{d}h}{\mathrm{d}t}. \qquad (7)$$

Boundary conditions at the conduit base, assuming a basal connection to a crack as depicted in Fig. 1, can be stated as

$$\begin{aligned} p|_{z=0} &= p_t, \\ u_z|_{z=0} &= -\frac{q}{A_c}. \end{aligned} \qquad (8)$$

where p_t is the pressure in the crack evaluated at the conduit junction, q is the volumetric flux from the conduit into the crack and $A_c = \pi R^2$ is the conduit cross-sectional area. p_t can be calculated by considering the mass balance at the base of the conduit

$$\frac{\mathrm{d}V_c \rho}{\mathrm{d}t} = -A_c \rho u_z, \qquad (9)$$

where V_c is the volume of the crack and ρ is fluid density. For long period oscillatory perturbations (much longer than L_x/c_0 with L_x a crack length and c_0 fluid sound speed), fluid compressibility effects are negligible compared to crack volume changes and Eqn (9) can be written as

$$\frac{\mathrm{d}p}{\mathrm{d}t}\bigg|_{z=0} = -\frac{A_c u_z}{C_t}. \qquad (10)$$

In Eqn (10), the storativity C_t is the characteristic response of the crack volume to a uniform opening pressure, neglecting inertia and viscous pressure drops within the crack. In general, it depends on both fluid and crack bulk moduli (Segall, 2010). However, the bulk modulus of water, K_f, is generally much larger than K_c and we neglect its effects here. Crack storativity may then be calculated as

$$C_t = \frac{\mathrm{d}V_c}{\mathrm{d}p}. \qquad (11)$$

The storativity of a symmetric crack can be represented in terms of the effective elastic modulus $G^* = G/(1 - \nu)$ of ice, with shear modulus G and Poisson's ratio ν, as well as crack length L_x and a constant κ

$$C_t = \kappa \frac{L_x^3}{G^*}. \qquad (12)$$

The scaling factor κ depends on the aspect ratio of the crack, a purely geometric quantity. It is found by calculating $\mathrm{d}V_c/\mathrm{d}p$ numerically using the displacement discontinuity method described above, combining Eqns (11) and (12) and solving for κ. $\mathrm{d}V_c/\mathrm{d}p$ is found by applying a uniform pressure to the crack and calculating change in volume. For glacial parameters (Table 1), $\kappa = 0.4814 \pm 0.0006$ with respect to the variable crack length. Note that Eqn (12) is strictly valid only for cracks in a homogeneous elastic half space. To find pressure at the crack mouth p_t we integrate Eqn (10) in time. For low-frequency perturbations the fluid is essentially incompressible, and p_t can then be written using Eqn (7) as

$$p_t = -\frac{A_c h}{C_t}. \qquad (13)$$

For high-frequency perturbations, there is no flux into the crack and the conduit bottom becomes a constant velocity boundary condition, $u_z = 0$. When cracks intersect the conduit between the surface and its base, conservation of fluid momentum and mass at the crack mouth gives rise to additional frequency dependent junction conditions.

Governing equations: fluid-filled crack

For the crack, we consider a 3-D tabular cavity defined by the coordinate system x, y and ξ, where ξ represents the direction of opening for the crack as seen in Fig. 1. We use width-averaged equations for fluid flow in a 3-D crack (Lipovsky and Dunham, 2015; Liang and others, 2020):

$$\rho_0 \frac{\partial u_x}{\partial t} + \frac{\partial p}{\partial x} = \langle \nabla \cdot \tau \rangle_x, \qquad (14)$$

$$\rho_0 \frac{\partial u_y}{\partial t} + \frac{\partial p}{\partial y} = \langle \nabla \cdot \tau \rangle_y, \qquad (15)$$

$$\frac{1}{\rho_0} \frac{\partial \rho}{\partial t} + \frac{\partial u_x}{\partial x} + \frac{\partial u_y}{\partial y} + \frac{1}{w_0} \frac{\partial w}{\partial t} = 0, \qquad (16)$$

$$\frac{1}{\rho_0} \frac{\partial \rho}{\partial t} = \frac{1}{K_f} \frac{\partial p}{\partial t}, \qquad (17)$$

where w is the perturbed crack opening in reference to the crack center-line (perpendicular to the unperturbed opening dimension w_0). Width-averaged velocities u_x and u_y in the crack are expressed as

$$u_i(x, y, t) \equiv \langle v_i \rangle = \frac{1}{w_0} \int_0^{w_0} v_i(x, y, \xi, t) \mathrm{d}\xi \qquad (18)$$

with $i = x$, y. Similar to the conduit, we assume fully developed flow in the crack for our numerical experiments, in which case

the shear stress terms become

$$\langle \nabla \cdot \tau \rangle_i = \frac{12\mu}{w_0^2} u_i. \tag{19}$$

To close our system of crack equations, we apply no slip boundary conditions on the crack faces and zero normal velocity boundary conditions at the edges of the crack.

The non-local response of crack walls to pressure perturbations is modeled with quasi-static elasticity, using the displacement discontinuity method (Crouch and others, 1983; Okada, 1985). This involves discretizing the crack into rectangular elements subject to opening-mode displacements, which are stitched together to ensure displacement and stress continuity (Liang and others, 2020). A symmetric and positive definite stiffness matrix K_s then relates crack opening $\mathbf{w}(x, y, t)$ and pressure $\mathbf{p}(x, y, t)$ on the mesh to evaluate Eqn (16), as

$$\mathbf{p} = K_s \mathbf{w}. \tag{20}$$

We also use K_s to calculate the crack effective bulk modulus, which is defined as

$$\frac{1}{K_c} = \frac{1}{V_{c,0}} \frac{dV_c}{dp}, \tag{21}$$

where $V_{c,0} = L_x L_y w_0$ is a reference volume and dV_c/dp is approximated numerically as discussed above.

Coupling between conduit and crack

To simulate fluid flow between conduit and crack elements, we couple the conduit and crack system of equations through pressure continuity and a discontinuous jump in the velocity due to the flux q into and out of the crack across each coupling point z_c:

$$p(z_c^+, t) - p(z_c^-, t) = 0, \tag{22}$$

$$q(z_c^+, t) - q(z_c^-, t) = -A_f u_z(z_c, t), \tag{23}$$

where $A_f = 2\pi R w_0$ is the cross-sectional area of the crack intersecting the conduit assuming crack dip is 0 °. For dipping cracks the effective area increases with increasing dip as explained below.

Next, we incorporate the volume exchange between components and crack elasticity into the governing equations. Assuming wavelengths of the perturbation are long compared to the crack opening, and combining Eqns (16), (17) and (20) we get

$$\frac{1}{\bar{K}} \frac{\partial p}{\partial t} + \frac{\partial u_x}{\partial x} + \frac{\partial u_y}{\partial y} = \frac{q}{w_0} \delta(x - x_c) \delta(y - y_c), \tag{24}$$

where $1/\bar{K} = 1/K_c + 1/K_f$ and q is the fluid flux into the crack from the conduit. The fluid flux is modeled as a point source excitation with a delta function $\delta(x - x_c) \delta(y - y_c)$ at the coupling point (x_c, y_c) of the conduit in the crack coordinate system. This delta function is scaled by the calculated energy transfer from the conduit into the crack seen in the right-hand-side of Eqn (24).

If a crack is dipping at some angle θ with respect to the conduit, the energy exchange between the conduit and crack will change as the cross section becomes elliptical instead of circular. We account for this area change using an effective circular radius (Tang and Cheng, 1993). If we consider the semi-minor axis of

the ellipse equal to the conduit radius, the semi-major axis can be written as

$$R_1 = \frac{R}{\cos(\theta)} + \frac{w_0 \tan(\theta)}{2}, \tag{25}$$

using the ellipticity $e_E = \sqrt{R_1^2 - R^2}/R_1$, we can write the effective radius as

$$R_e = \frac{2}{\pi R_1 E(e_E, \pi/2)}, \tag{26}$$

where $E(e_E, \pi/2)$ is the complete elliptic integral of the second kind: $E(k, \theta) = \int_0^\theta \sqrt{1 - k^2 \sin^2(\theta')} d\theta'$.

Excitation of wave motion

Natural excitation of oscillatory flows in the englacial environment could arise from impulsive sources (Gräff and others, 2019) or continuous sources (Roeoesli and others, 2016). We largely focus on the impulsive case for this study and use a Gaussian pressure pulse applied at the water surface to perturb our system

$$P_{source}(t) = P_0 e^{-(1/2)(t/\Delta T)^2}, \tag{27}$$

with amplitude P_0 and half width ΔT. Due to the linearity of our problem, we assume unit forcing $P_0 = 1$ Pa in this study. A wavelength scale for the Gaussian function is calculated as $\lambda_{ex} = c_T \times \Delta T$ where ΔT is the full width at half maximum of the Gaussian in the time domain (Eqn (27)) and c_T is the tube wave speed (defined in the next section). We note that Eqn (27) is used for its relative simplicity, but other impulsive excitation functions might be used to narrow the input frequency range, such as a chirp signal.

Numerical implementation

We solve the coupled system of equations using a 6th-order summation-by-parts finite difference scheme in space and a 4th-order Runge–Kutta method in time (O'Reilly and others, 2017). Boundary conditions in the conduit are weakly enforced using simultaneous approximation terms (Del Rey Fernández and others, 2014; Erickson and others, 2019) and boundary conditions in the crack are strongly enforced. Pressure and velocity in the conduit are solved on regular collocated grids, while the crack requires velocity grids to be staggered with respect to the pressure grids to prevent a coordinate singularity at the crack center (Prochnow and others, 2017). To maintain stability and high-order accuracy, the viscosity term in Eqns (3), (14) and (15) are solved implicitly in time (Liang and others, 2020).

Results

Interpreting resonant oscillations

The characteristics of eigenmodes depend on the geometry of the resonating structure, the fluid properties and the source–time function of excitation (e.g. Biot, 1952; Krauklis, 1962). We focus on the characteristic frequencies of eigenmodes here as a discriminator, noting that eigenmode damping rate and resulting time-dependent deformation patterns in the ice, if detectable, provide additional information.

In tube-like geometries, interface waves or 'tube waves' can involve either local or non-local elastic coupling to the fluid (Burridge and others, 1993; Sheriff and Geldart, 1995). In this study, we focus on long wavelength excitation compared to the

conduit radius, in which conduit walls deform quasi-statically and a non-dispersive compressional wave results. The tube wave travels along the fluid–solid interface at a slightly slower speed than the acoustic wave speed (Biot, 1952). For a straight circular borehole, this speed is

$$c_{\mathrm{T}} = \sqrt{\frac{1}{\rho_0}\left(\frac{1}{K_{\mathrm{f}}} + \frac{1}{G}\right)^{-1}}. \tag{28}$$

In this study, we neglect the effects of borehole along-axis curvature and cross-sectional ellipticity. However, natural englacial conduits can be sinuous along their axis and elliptical in cross section. These effects modify the long wavelength tube wave speed by changing the compliance of the borehole (Norris, 1990; Burridge and others, 1993).

Tube waves in the conduit will resonate at 'organ pipe' frequencies. These resonant frequencies depend on the tube wave speed, the boundary conditions – whether the ends of the pipe are considered open or closed – and the conduit length (Lighthill, 1978)

$$f_{\mathrm{open/open}} = \frac{nc_{\mathrm{T}}}{2L}, \tag{29}$$

$$f_{\mathrm{closed/open}} = \frac{mc_{\mathrm{T}}}{4L}, \tag{30}$$

Here, $n = 1, 2, 3\ldots$ and $m = 1, 3, 5\ldots$ are integer harmonic numbers. For example, a vertical englacial conduit connected to a large cavity could resonate like an organ pipe open at both ends since both the conduit top and bottom are free pressure boundaries. Conversely, a conduit terminating at the base of a glacier is equivalent to an organ pipe with one end open (free surface at the top of the conduit) and one end closed (solid boundary at the bottom of the conduit).

Crack waves, also known as Krauklis waves, are a type of interface wave that manifest in fluid-filled cracks where one dimension is small compared to the other two (Krauklis, 1962; Ferrazzini and Aki, 1987). Crack waves involve coupled fluid and elastic solid motion and are excited when perturbation wavelengths exceed the scale length for elastic coupling (e.g. Dunham and Ogden, 2012). For high-frequency perturbations, the crack will respond rigidly to perturbations and crack waves will not be excited. At low frequencies, crack walls become more compliant and crack waves will manifest resulting in lower phase velocities with decreasing frequency. Crack wave dispersion manifests as unequal spacing of resonant harmonics in a crack. Lipovsky and Dunham (2015) estimated the frequency spacing between crack wave modes as $f_n/f_1 = n^{3/2}$.

We calculate crack wave frequencies using the normalized crack impedance, which is a transfer function between pressure and fluid velocity at the crack mouth

$$F(\omega) = \frac{1}{\rho_0 c_0}\frac{\hat{p}(0, \omega)}{\hat{u}_z(0, \omega)}, \tag{31}$$

where $\hat{p}$ and $\hat{u}_z$ are the Fourier transformed pressure and velocity. The Fourier transform and its inverse are defined as

$$\hat{\Phi}(\omega) = \frac{1}{2\pi}\int_{-\infty}^{\infty}\Phi(t)e^{-i\omega t}\mathrm{d}t,$$
$$\Phi(t) = \int_{-\infty}^{\infty}\hat{\Phi}(\omega)e^{i\omega t}\mathrm{d}\omega. \tag{32}$$

Note that we define the normalized crack impedance as the inverse of the crack transfer function in Liang and others (2017). Frequencies where $|F(\omega)|$ is maximized represent the most efficient exchange between the crack and conduit for crack waves.

Coupled wave motion

In addition to crack and tube wave modes, coupled resonant modes exist between the conduit and crack. One mode, identified as the 'conduit reservoir mode' in Liang and others (2020), will be referred to as the 'coupled mode' here. For the coupled mode, fluid may be considered incompressible in the conduit, allowing the entire fluid column to oscillate under the influence of gravity in and out of the elastic crack. Liang and others (2020) derived this resonant frequency accounting for fluid density stratification in the conduit. We assume constant density here, however, we will generalize the modeling of this mode by analytically solving for non-fully developed flow regimes in the conduit.

Starting from our linearized momentum balance in the conduit, we integrate Eqn (3) in the incompressible limit from $z = 0$ to L:

$$\rho_0\frac{\partial u_z}{\partial t} + \frac{1}{L}\left[p_L - p_0\right] = \frac{1}{L}\int_0^L \langle\nabla\cdot\tau\rangle_z\mathrm{d}z. \tag{33}$$

For fully developed flow, the shear stress term $\langle\nabla\cdot\tau\rangle_z$ is Eqn (5) and does not depend on conduit length or frequency. However, in the boundary layer limit this shear stress term is more complicated. To determine the shear stress term, we use the solution of Womersley (1955) for flow in a tube subject to a driving pressure variation $\partial p/\partial z$ that is harmonic in time with frequency ω. The resulting velocity is

$$v_z = \mathrm{Re}\left[\frac{1}{i\rho_0\omega}\frac{\partial p}{\partial z}\left\{1 - \frac{J_0(\alpha(r/R)i^{3/2})}{J_0(\alpha i^{3/2})}\right\}\right], \tag{34}$$

where $\alpha(\omega) = R\sqrt{\omega\rho_0/\mu}$ and J_i are Bessel functions of the first kind, order i. Using the identity $\int_0^\psi \psi' J_0(\psi')\mathrm{d}\psi' = \psi J_1(\psi)$, the cross-sectionally averaged velocity is

$$u_z = \langle v_z \rangle = \mathrm{Re}\left[\frac{1}{i\omega\rho_0}\frac{\partial p}{\partial z}\left(1 - \frac{2}{\psi}\frac{J_1(\psi)}{J_0(\psi)}\right)\right], \tag{35}$$

where for notational convenience $\psi(\omega) = \alpha(\omega)\,i^{3/2}$. Shear stress may then be computed using the Bessel function recurrence relation $(2m/\psi)\,J_m(\psi) = J_{m+1}(\psi) + J_{m-1}(\psi)$ as

$$\langle\nabla\cdot\tau\rangle_z = -\mathrm{Re}\left[\psi\frac{2\mu}{R^2}\frac{J_1(\psi)}{J_2(\psi)}u_z\right]. \tag{36}$$

Assuming quasi-static opening of the crack, if we substitute Eqns (6) and (13) into Eqn (33) and rewrite in terms of the cross-sectionally averaged fluid displacement (Eqn (7)), we obtain the equation of a damped harmonic oscillator

$$\frac{\mathrm{d}^2h(t)}{\mathrm{d}t^2} + \omega_0^2 h(t) + 2\rho_0 L\gamma\frac{\mathrm{d}h(t)}{\mathrm{d}t} = 0, \tag{37}$$

with natural frequency

$$\omega_0 = \sqrt{\frac{g}{L}\left(1 + \frac{A_{\mathrm{c}}}{\rho_0 g C_t}\right)} \tag{38}$$
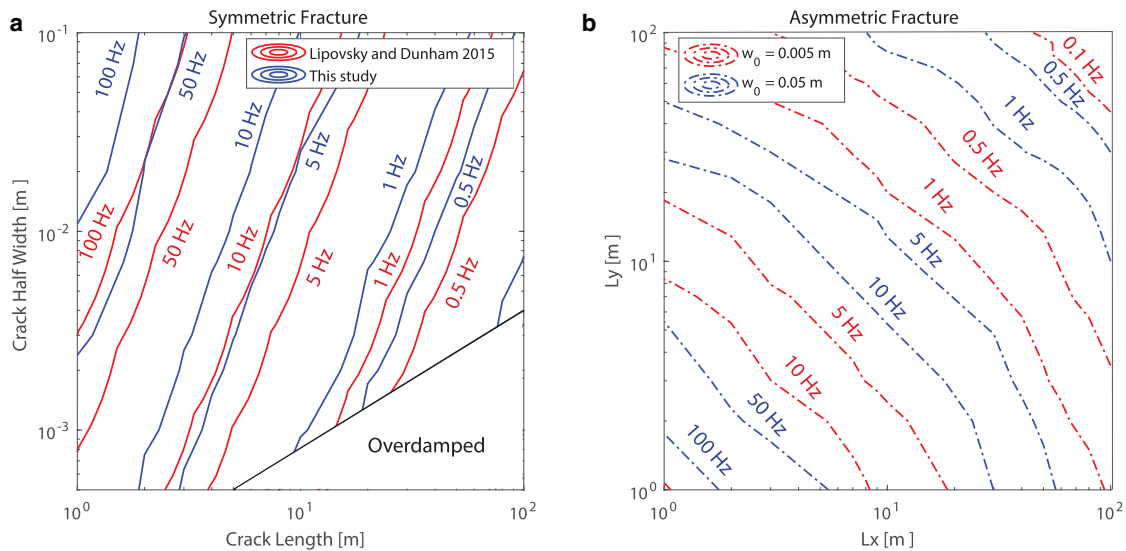
Fig. 2. Fundamental crack resonant frequencies for symmetric and asymmetric cracks. (A) Fundamental mode of a symmetric tabular crack, comparing the 2-D model (one length dimension and opening) of Lipovsky and Dunham (2015) (red contours) to the 3-D model studied here (blue contours). The over-damped region is determined from Lipovsky and Dunham (2015); no resonance occurs in this part of parameter space. (B) Variation of the fundamental mode for an asymmetric 3-D crack for two different crack length dimensions L_x and L_y. Where red contours represent a crack thickness of 0.005 m and blue contours represent results for a crack thickness of 0.05 m. Undulations in the contours reflect finite numerical resolution of crack storativity, leading to ∼5% uncertainty in crack dimensions.

and damping coefficient

$$\gamma = \frac{\mu}{\rho_0 R^2} \psi \frac{J_1(\psi)}{J_2(\psi)}. \qquad (39)$$

For an under-damped harmonic oscillator the resulting resonant frequency can be calculated as

$$\omega = \sqrt{\omega_0^2 - \gamma^2}, \qquad (40)$$

and the quality factor can be calculated as the energy stored divided by the energy lost in one oscillation

$$Q = \frac{\omega}{2\gamma}. \qquad (41)$$

If we consider the fully developed limit $\psi \ll 1$, so $J_m(\psi) \to (\psi/2)^m (1/(\Gamma(m+1)))$ with $\Gamma(x)$ the Gamma function, Eqn (39) loses its frequency dependence:

$$\gamma_{\text{dev}} = 4\frac{\mu}{\rho_0 R^2}. \qquad (42)$$

If we neglect viscosity, Eqn (37) becomes a simple harmonic oscillator and the coupled mode frequency reduces to the natural frequency (Eqn (38)).

This coupled mode is derived for a crack intersecting at the base of a conduit, however a similar oscillation can arise in a system with a crack intersecting anywhere along the conduit. In that case, we must account for partitioning of flow between the crack and the conduit based on the relative cross-sectional areas of the crack opening and the conduit. It is standard to express this energy exchange in terms of reflection and transmission coefficients (Lighthill, 1978). For our system we use reflection and transmission coefficients similar to those derived in Liang and others (2017):

$$R(\omega) = -\frac{1}{1 + 2\chi F(\omega)} \qquad (43)$$

$$T(\omega) = \frac{2\chi F(\omega)}{1 + 2\chi F(\omega)} \qquad (44)$$

where $\chi = (c_0/A_f)/(c_T/A_c)$. These reflection and transmission coefficients are frequency dependent, implying selective interactions of the crack with oscillatory flow in the conduit. In addition, Eqn (26) implies that A_f increases with crack dip, such that $|R| \to 1$ and flux into the crack is maximized as dip angle $\theta \to 90°$.

Numerical experiments

Here, we present and analyze model results based on the theory and numerical approach outlined in the previous sections to explore which resonant modes might manifest in typical englacial systems, and how appropriate interpretation of frequency spectra could lead to inference of hidden transport geometries. We first present our analysis of crack resonance in isolation to connect with previously published study, then we study wave motion in three coupled englacial geometries: a conduit connected to a basal crack, a conduit connected to a crack located somewhere between the surface and the base and finally a multi-crack system.

We excite wave motion in our numerical experiments by initiating a pressure pulse at the water surface, then analyze fluid pressure and particle velocity time series at locations in the conduit and in the crack. Frequency domain analysis permits an interpretation of the resulting power spectrum to infer the resonant frequencies in the system. All model parameters for our englacial system can be found in Table 1 and were informed by studies of conduits and cracks in the englacial system (Anandakrishnan and Alley, 1997; Vatne, 2001; Petrenko and Whitworth, 2002; Fountain and others, 2005; Catania and others, 2008; West and others, 2010).

Crack resonance

We first focus on fluid resonance in cracks alone. Lipovsky and Dunham (2015), assuming a symmetric 2-D crack, showed that the period and quality factor (energy loss over an oscillation cycle) for the fundamental resonant mode of a crack may be used to infer crack length and opening. We reproduced their calculation in Fig. 2A (red contours), demonstrating that an
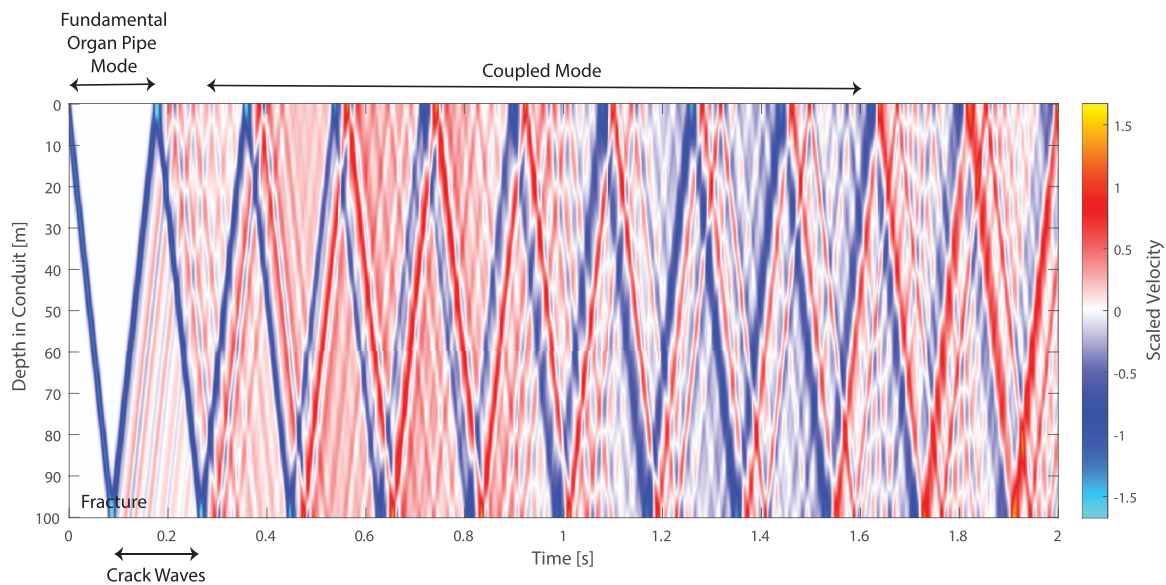
Fig. 3. Fluid particle velocity (u_z) throughout the conduit in time, for a basal crack system with conduit length $L = 100$ m, radius $R = 10$ cm, a symmetric crack of length $L_x = 5$ m and opening of $w_0 = 1$ cm. The center of the Gaussian excitation pulse is at 0 s model time with a scaled wavelength of 10 m. Following excitation we follow the propagating tube wave down the conduit until it reaches the basal crack at 100 m. When the tube wave reaches the crack, most of the energy is reflected and subsequently resonates at the fundamental organ pipe frequency. Energy that enters the crack is transmitted back into the conduit in the form of crack waves (first seen from $\sim$0.1–0.3 s). Although wave motion becomes more complex through time, we note a full conduit velocity polarity change at $\sim$1–1.2 s. This bulk motion in the fluid shows the long period coupled mode in the basal crack system.

extension to two length dimensions (a 3-D tabular crack) is comparable in the symmetric case (Fig. 2A). We note that the overdamped region is determined from the Lipovsky and Dunham (2015) analysis of quality factor. We do not consider boundary layer effects in the crack and thus generally underpredict quality factor for the crack in our model. Across this range of crack dimensions, fundamental frequencies derived from our 3-D simulations are up to two times smaller than in the 2-D simulations presented in Lipovsky and Dunham (2015).

In the englacial environment, cracks are likely to be asymmetric in their length dimensions. Figure 2B shows that crack asymmetry can result in non-unique fundamental frequencies. For example, if we consider a crack length of $L_x = 10$ m, and a crack opening between 5 and 50 mm, the fundamental frequency could vary between 0.4 and 30 Hz depending on L_y. This non-uniqueness implies that higher order eigenmodes are required to constrain both length scales of an asymmetric crack.

Basal crack

We next consider a coupled geometry with a conduit connected to a crack at its base. This models a moulin or borehole connected to a crack at its base. For the calculations and model results shown below we consider a 100 m conduit with a 10 cm radius, similar to a borehole, and a symmetric basal crack of length $L_x = 5$ m with an opening of 1 cm. We excite the system with a scale wavelength ($\lambda_{ex} = c_T/\Delta T$) of 10 m or $\Delta T = 0.0075$ s (Eqn (27)), following the crack resonance condition from Lipovsky and Dunham (2015).

Figure 3 shows a spatial time series of the water particle velocity (u_z) in response to a pressure perturbation at the water surface, where velocity is scaled by the characteristic fluid pressure magnitude, $v_{scaled} = (\rho_0\, c/P_0)\, v_z$. This figure highlights how the surface pressure perturbation affects the overall fluid motion in the conduit through time. Multiple wave modes are evident but somewhat complicated to disentangle in the time domain. However, in the frequency domain these modes and their harmonics are easily distinguished. In Fig. 4, we show pressure time series and spectra associated with the simulation in Fig. 3. Figures 4A and 4B show how pressure changes through time in the conduit

and the crack. Figure 4D shows the fast Fourier transform (FFT) of a pressure time series taken at 50 m down the conduit shown in Fig. 4C. In this time series, we see organ pipe modes and harmonics beginning at 5.6 Hz, three crack wave modes at 41, 68 and 103 Hz, and the coupled mode at 0.75 Hz corresponding to the fundamental eigenmode of the system. Crack modes correspond to the peaks in the normalized crack impedance defined in Eqn (31), seen in Fig. 4E.

The power spectrum for the basal crack case shows that the coupled mode has the highest amplitude of all modes shown in the conduit. High amplitude modes are most likely to be measurable in the field, as has been observed in the volcanic setting (Chouet and Dawson, 2013). We therefore now focus on this coupled mode as a possible tool for englacial geometric inference and consider both fully developed and boundary layer effects. We first note that the inviscid frequency Eqn (38) has two limits associated with distinct restoring forces for the oscillation. If $A_c/\rho_0\, C_t\, g \gg 1$, the frequency of the coupled mode does not depend on gravity and equals $f_{el} = (1/2\pi)\sqrt{(A_c/\rho_0 C_t)/L}$. For $A_c/\rho_0\, C_t\, g \ll 1$, Eqn (38) reduces to a gravity-dependent limit, $f_g = \sqrt{g/L}$ where crack elasticity no longer matters. Figure 5 shows how the coupled mode frequency and the damping rate scale for the full range of englacial parameters described in Table 1. The x-axis of Fig. 5A illustrates data collapse as the wavelength associated with the elastic limit frequency, λ_{el}, is $\lesssim 1$. For $\lambda_{el}/L \gg 1$, the data collapse onto the gravity-dependent frequency f_g plotted as the dashed lines in Fig. 5A. The gravity-dominated limit does not depend on crack parameters and thus it is not possible to determine crack geometry when in this limit.

Quality factor for the coupled mode (Eqn (41)) depends on resonant frequency ω and frequency-dependent damping rate γ (ω) but not on flow inside the crack. Crack geometry enters the coupled mode only through the crack storativity, which does not constrain opening w_0. Dissipation is thus governed by flow in the conduit, where the low viscosity of water implies that flow may not be fully developed at the periods of interest. Figure 5B shows that the coupled mode for glacial parameters mostly falls in the boundary layer limit. Fully developed flow is
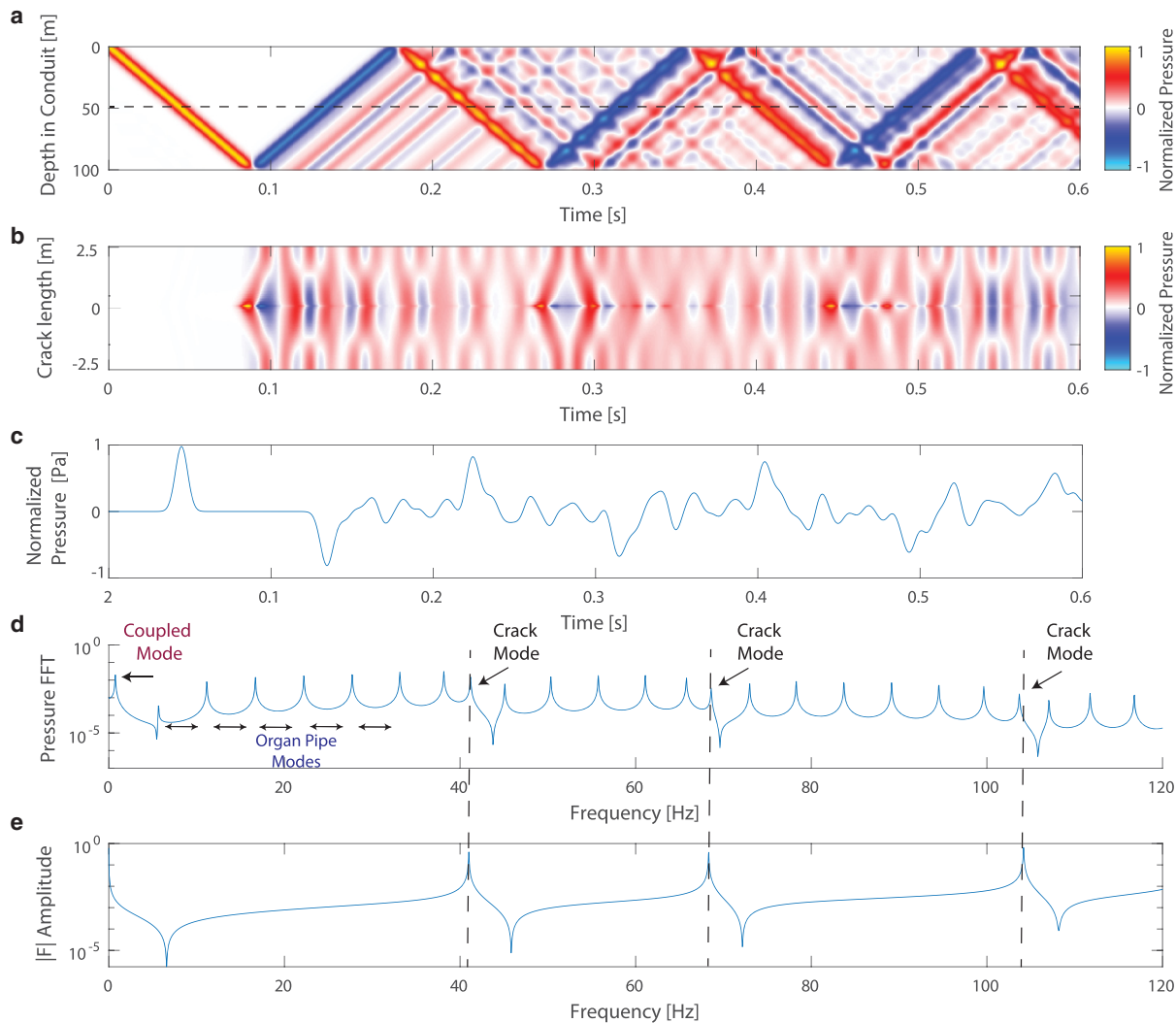
Fig. 4. Spatial time series and frequency spectra for resulting wave motion in an englacial geometry with a conduit connected to a basal crack (assuming fully developed flow). (A) Similar to Fig. 3 but showing pressure time series throughout the conduit–crack network. (B) Spatial time series in the crack. (C) Pressure time series in the conduit taken at 50 m depth noted as the dashed line in panel (A). (D) Frequency spectrum of the time series shown in (C). In this frequency spectra, we note the coupled frequency at 0.75 Hz, crack wave modes at frequencies 41, 68 and 103 Hz, and many harmonics of the fundamental organ pipe frequency at 5.6 Hz. (E) Normalized crack impedance $|F|$ for the basal crack, where $|F|$ maxima correspond to observed crack wave frequencies in the conduit.
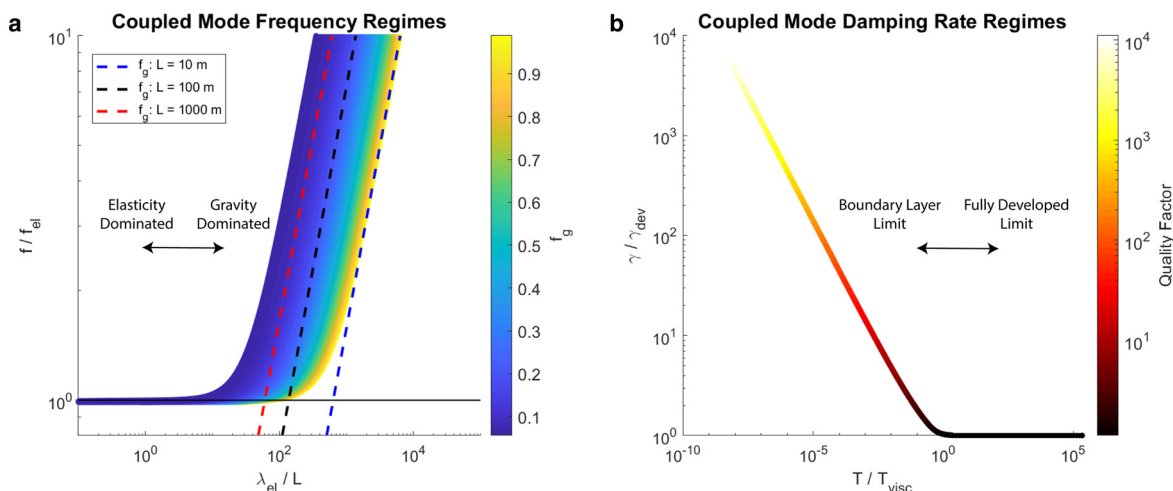
Fig. 5. Coupled mode frequency and damping rate regimes. (A) Dominant restoring force as a function of frequency f for the coupled mode in a basal crack system. In the elastic limit, the coupled mode frequency is $f_{el} = (1/2\pi)\sqrt{(A_c/\rho_0 C_t)/L}$, while in the gravity limit frequency follows $f_g = (1/2\pi)\sqrt{g/L}$. The x-axis shows the wavelength $\lambda_{el} = c_T/f_{el}$ normalized by conduit length L. The dashed lines represent the gravity limit frequency for three different conduit lengths of 10, 100 and 1000 m. This highlights where the data collapse onto the gravity limit. (B) Quality factor of the coupled mode is controlled by the ratio of mode period and momentum diffusion time across the conduit $T_{visc} = R^2 \rho_0/\mu$. The y-axis shows cross-sectionally averaged shear stress in the conduit (Eqn (39)) normalized by the fully developed limit $\gamma_{dev} = 4\mu/\rho_0\,R^2 = 4/T_{visc}$. This illustrates the importance of a boundary layer treatment of viscous damping for assessing quality factors in the glacial environment.
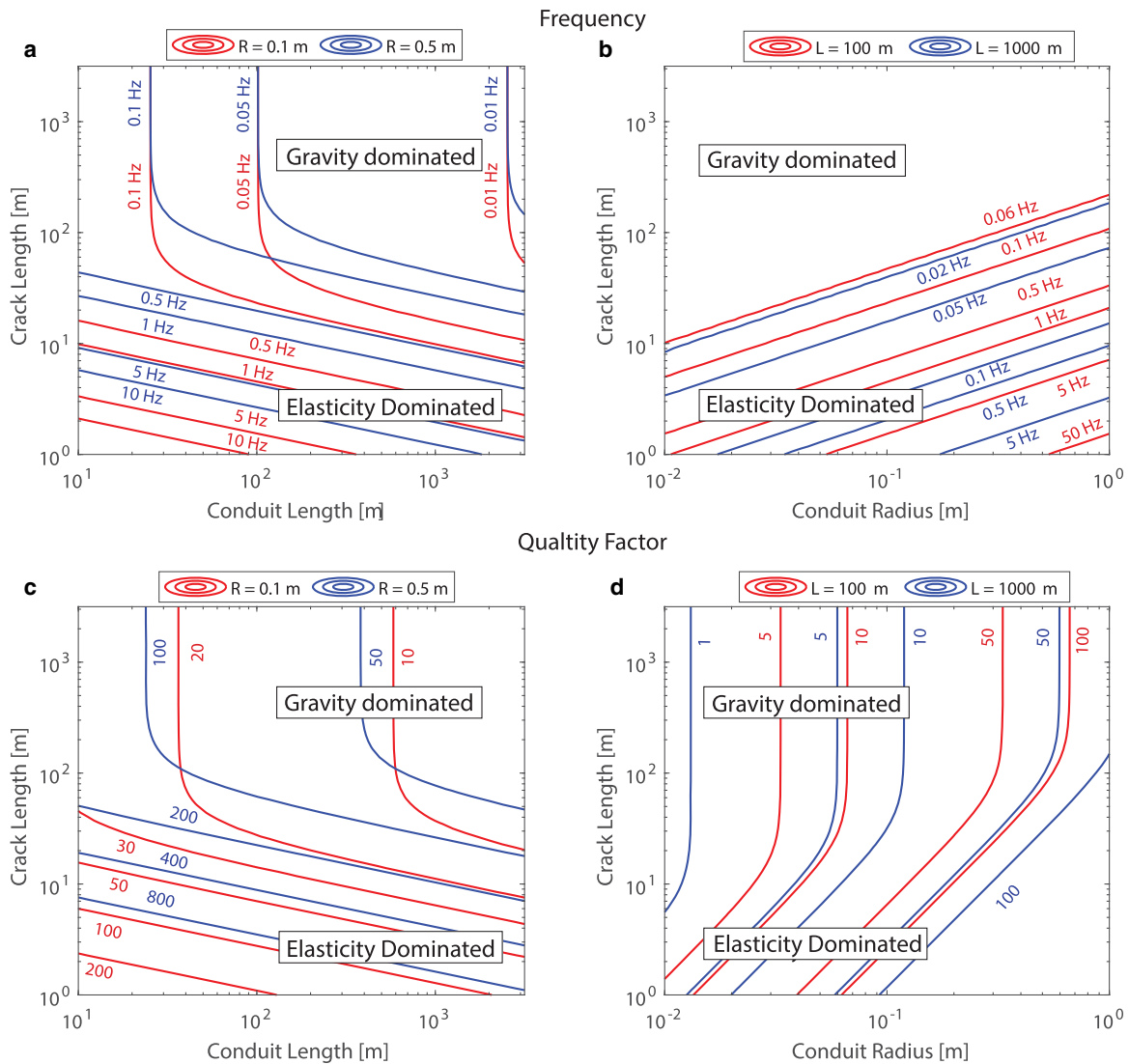
Fig. 6. Coupled mode frequency and quality factor for the range of glacial parameters in Table 1. (A and B) Frequency contours for $R = 0.1$ and 0.5 m, and $L = 100$ and 1000 m. (C and D) Quality factor contours for $R = 0.1$ and 0.5 m, and $L = 100$ and 1000 m. In all panels, transitions to the gravity-dominated limit can be seen where the frequency and quality factor lose crack length dependence. Panel (B) in particular shows no frequency variation for crack lengths above the 0.06 Hz (red) and 0.02 Hz (blue) contour. Conduit lengths and radii were chosen as proxies for an alpine and ice-sheet environment.

only a valid assumption for small conduit radii and long conduit lengths.

We can determine the crack length from the coupled mode using both the quality factor and frequency. We first note that for very large cracks our model assumption of a uniform opening pressure in the crack breaks down. Using Eqns (40) and (41), we take 2-D slices through the 3-D parameter space (L, L_x, R) to plot crack length versus period and conduit length, and contour both the frequency and quality factor as shown in Fig. 6. Alternatively, if one knew the conduit radius or conduit length and the frequency or quality factor, the crack length could be determined using a graphical approach similar to Fig. 6, with parameters tailored to the specific case.

Middle crack
Next we examine a crack located between the base of the conduit and the surface. Using the same parameters as the basal cavity case, we place a horizontal crack 30 m from the base of the conduit. Figures 7A and 7B show these results for the fully developed limit. Similar to the basal crack geometry, we see organ pipe modes (in both conduit sections, due to reflection and transmission of energy past the crack mouth) as well as crack wave modes

and a coupled mode. The organ pipe mode associated with the top conduit section is ~8 Hz and is associated with a pipe open at both ends (Eqn (29)). The organ pipe frequency associated with the bottom conduit section is ~9 Hz, and is equivalent to a pipe open at one end and closed at the other (Eqn (30)). The difference in these modes is due to the no slip boundary condition at the conduit base versus the pressure boundary condition at the crack and conduit interface. We also see a coupled mode associated with flow from upper section of the conduit in and out of the crack as the fundamental mode. We do not see a coupled mode associated with the bottom section of the conduit because it is closed to flow in the incompressible limit. Finally, we see the same crack modes as those in the basal case since the crack dimensions have not changed. The crack impedance used to identify these modes is the same as that in Fig. 4D.

The middle crack geometry provides an ideal test bed for the role of crack dip. Englacial cracks are often observed to be dipping at fairly steep angles, ~70° (Fountain and others, 2005). Figure 8 shows how dip angle affects the reflection and transmission of waves, using the same crack geometry as all previous experiments. The normalized crack impedance for this crack is shown in Fig. 4E and is used to calculate the reflection
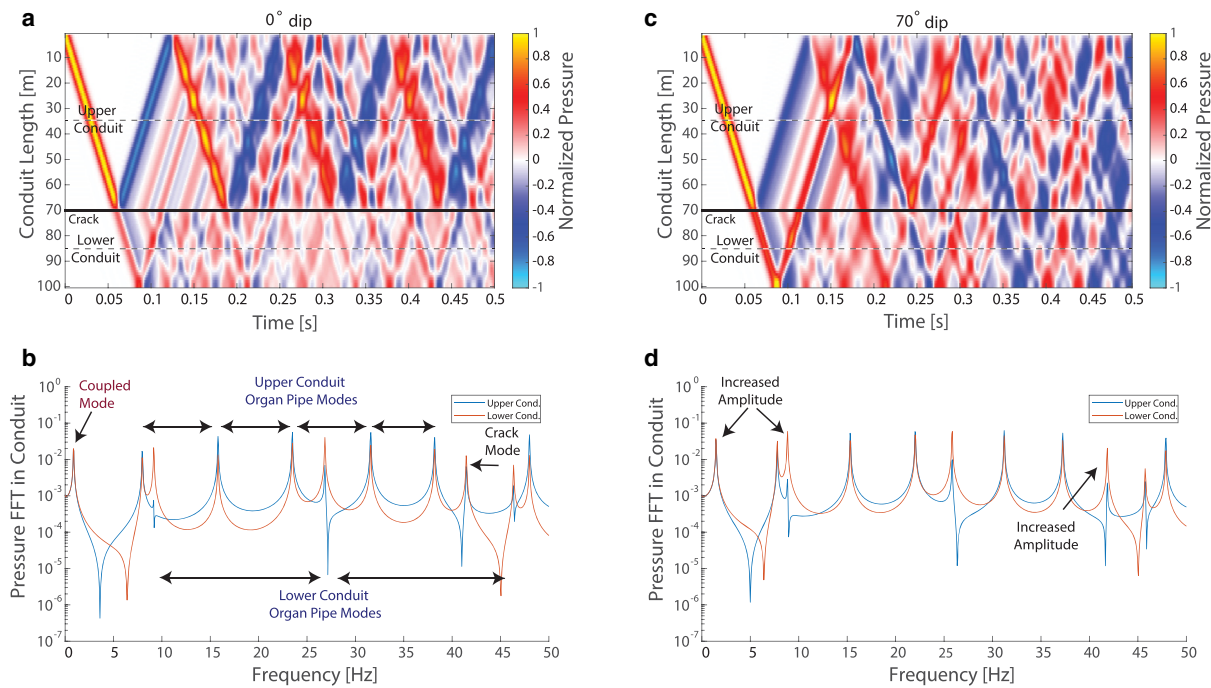
Fig. 7. Spatial time series and frequency spectra for two middle crack models with the same geometric parameters and forcing as the coupled basal crack simulation in Fig. 4, except that the crack is located at 70 m down the conduit and varies in dip between the two simulations. (A) Spatial time series for a crack dipping at 0°. (C) Spatial time series for a crack dipping at 70°. (B) Frequency spectra for a crack dipping at 0°. (D) Frequency spectra for a crack dipping at 70°. The thick black line in (A) and (C) represents the location of the crack and the gray dashed lines represent the location of the time series in the upper and lower conduits that are Fourier transformed to create the spectra in (B) and (D).
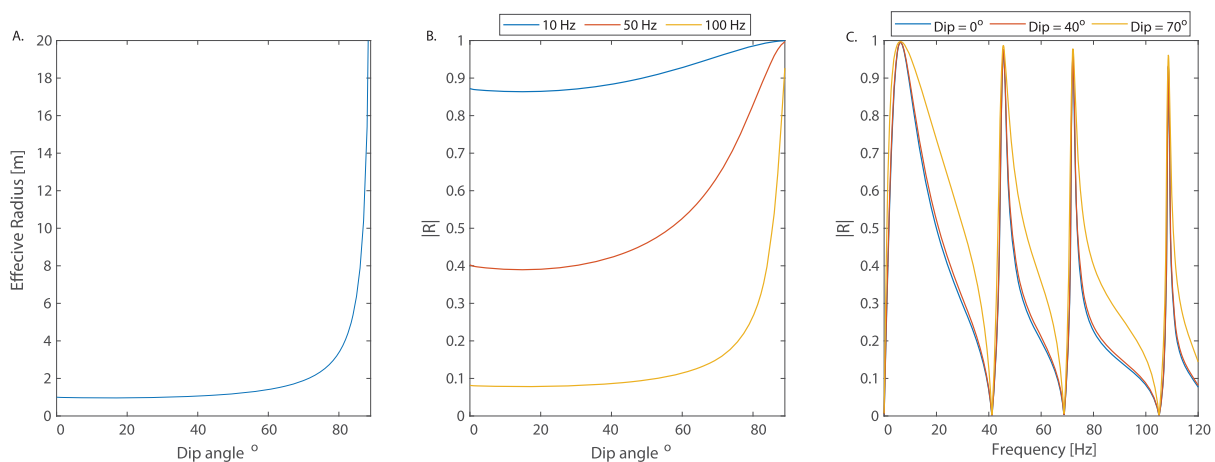
Fig. 8. Effects of crack dip angle. (A) Role of crack dip on effective radius of a tabular crack intersecting a central conduit. (B and C) Variation of reflection coefficient (Eqn (43)) with dip angle and frequency, geometric parameters similar to Fig. 7.

coefficient from Eqn (43), using effective radius for the crack area from Eqn (26).

Figures 8B and 8C show that the reflection coefficient increases with increasing dip angle, becoming largest for angles $\gtrsim 75°$. The reflection coefficient is frequency dependent and controlled by the crack impedance. Fluid flux into the crack is determined as jump in flux across the crack, which is affected by the reflection and transmission coefficients as well as crack geometry.

These effects can be seen in Fig. 7 which compares a horizontal and 70° dipping crack at 70 m depth. Increased flux in the dipping case is reflected off of the crack tip and re-emitted to the conduit as stronger upward and downward propagating waves compared to the horizontal crack. The crack has a small length of 5 m compared to the incoming perturbation wavelength of $\sim$ 10 m, resulting in two-way transit within the crack before the

incoming wave has past. The increase in flux into and out of the dipping crack results in increased amplitude of the lower conduit organ pipe modes, coupled mode and crack modes (Figs 7B and D).

Multiple branching cracks

Finally, we present results from a multi-crack system to illustrate how the basic elements studied individually interact in a more complex englacial network. We consider three cracks located at depths of 40, 90 m and at the base of a 150 m long conduit. The cracks at 40 and 90 m have a length of 5 m whereas the crack at 150 m has a length of 10 m. The top crack at 40 m is dipping at a 70° angle and has an opening of 1 mm compared to 10 mm for the other two. All other model parameters are the same as previous experiments.
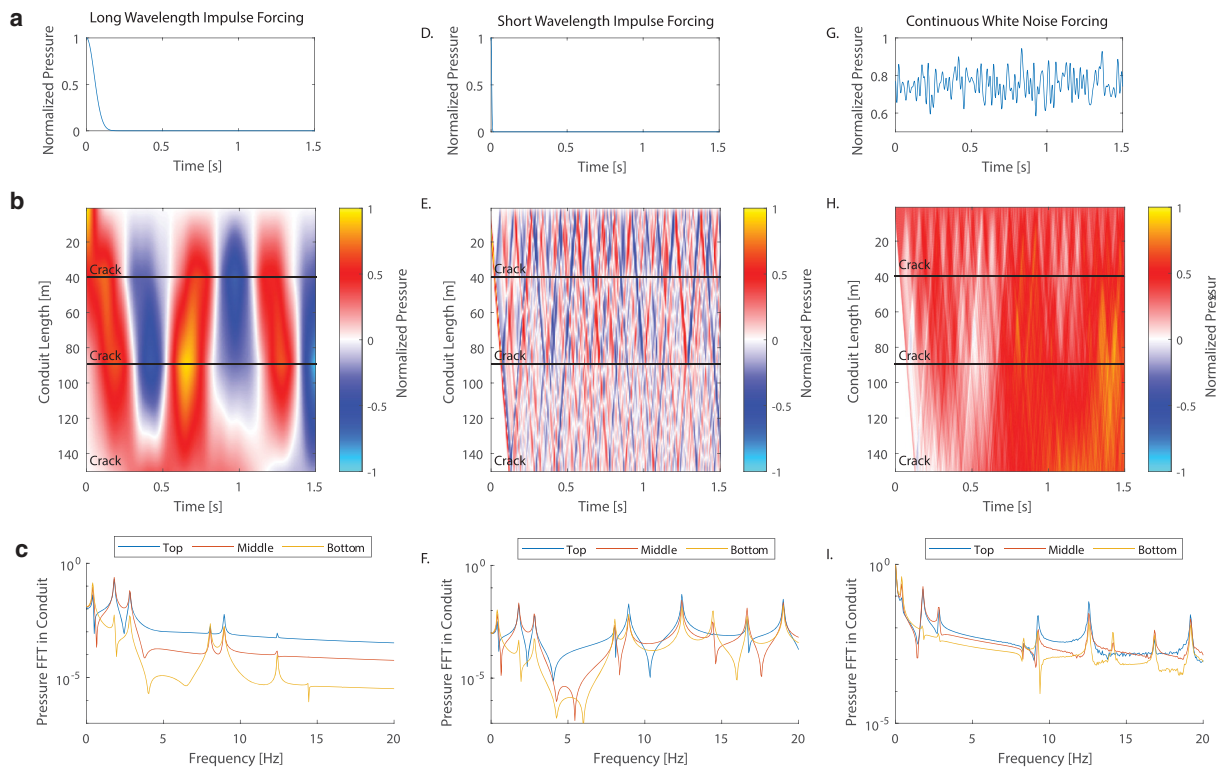
Fig. 9. Excitation of resonant modes from different source–time functions in a three crack system where the cracks are at depths of 40, 90 and 150 m. All other model parameters are the same as previous experiments and assuming fully developed flow. Left column: A long wavelength Gaussian excitation, with a scaled wavelength of 130 m. (A) Forcing function for the long wavelength model run. (B) Spatial time series for the long wavelength model run. (C) Frequency spectra for the long wavelength model run showing the FFT of time series taken at 20, 65 and 120 m. Middle column: A short wavelength excitation, with a scaled wavelength of 10 m. (D) Forcing function for the short wavelength model run. (E) Spatial time series for the short wavelength model run. (F) Frequency spectra for the short wavelength model run showing the FFT of time series taken at 20, 65 and 120 m. Right column: A simulated white noise continuous excitation, comprised of 2000 sine waves with random initial phase and a small amount of numerical noise. (G) Forcing function for the continuous forcing model run. (H) Spatial time series for the continuous forcing model run. (I) Frequency spectra for the continuous forcing model run showing the FFT of time series taken at 20, 65 and 120 m.

We use this example to illustrate the role of the pressure source–time function on eigenmode excitation. Figure 9 shows the results of three different multi-crack experiments, differing only in the form of $P_{\mathrm{source}}(t)$ in Eqn (6). The plots in the left column are for a system forced impulsively with $\Delta T = 0.05$ s or 130 m wavelength, and the plots in the center column are forced with $\Delta T = 0.0075$ s (10 m wavelength). The plots in the right column were forced continually with an excitation function comprised of 2000 sine waves with random initial phase and a small amount of numerical noise, normalized to unit maximum. The resulting quasi-white noise source–time function is a model for continuous excitation, for example from falling water in a moulin.

The conduit pressure frequency spectrum for each multi-crack system exhibits the same set of eigenmodes, excited to various degrees according to the forcing frequency spectra. The short wavelength excitation results in many resonant modes due to a broad range of excitation frequencies, while the long wavelength excitation preferentially excited low-frequency modes. The continuous forcing, while generating complex motions in the time domain, is still composed of a superposition of the same clearly identifiable eigenmodes.

In general, the amplitude of eigenmode excitation can be predicted directly from the frequency spectra of the source–time function given an appropriate transfer function (Karlstrom and Dunham, 2016). However we do not formulate such a transfer function here, or an explicit dependence on transport network complexity (e.g. number of cracks) as in Fig. 9. It is easy to imagine englacial geometries that are effectively unresolvable through fluid resonance measurements, such as a case when

branching cracks are spaced more closely than the wavelength of tube waves, but we leave this problem to future study.

Discussion

Increasing resolution and availability of measurement technologies have opened up new pathways toward discovery in most sub-disciplines of glaciology. Studies of water movement through glaciers and ice sheets are no exception having seen a burst of activity driven by the proliferation of seismologic and geodetic measurement in recent years (e.g. Kavanaugh and others, 2010; Roeoesli and others, 2016; Andrews and others, 2018; Rada and Schoof, 2018). The interpretation of such measurements relies on models. We have developed a quantitative framework to understand a class of unsteady fluid motions within glaciers and these resonant oscillations are controlled by the geometry and material properties of the hidden englacial transport network. Such signals could be detected by a range of geophysical measurements, including water pressure and seismicity time series. In this section we comment on the resolving power of the resonant modes of coupled conduit–crack networks, focusing on a coupled mode and conditions appropriate for alpine glaciers and ice sheets that are motivated by previously published data.

Detecting branching cracks from a conduit

We have investigated whether the geometry of branching cracks is encoded in low-frequency eigenmodes of a coupled conduit–crack network. This is motivated by the reasonable expectation that

lower frequency signals will be easiest to observe due to less attenuation and scattering for seismic measurements. However, we also recognize that low-frequency eigenmodes suffer some non-uniqueness when it comes to parameter resolving power. Therefore, we must assess whether sufficient geometric information is contained in low-frequency eigenmodes to be interesting.

Low-frequency eigenmodes and in particular the coupled mode constrain branching crack length in some circumstances, as illustrated in Fig. 6. Figure 5 shows that the coupled mode exhibits two regimes, a gravity-dominated regime and an elasticity-dominated regime. Crack geometry can be determined when elasticity matters, as seen in Fig. 6 where frequency and quality factor have power law dependencies over a broad range of crack lengths less than $L_x \sim 100$ m. The maximum detectable crack length increases for increasing borehole radius and decreasing conduit length, however it does not much exceed 100 m for reasonable glacial parameters. In addition, for quality factors $Q < 0.5$, the coupled mode is over-damped and will not generally encode a diagnostic period and quality factor. We find that the coupled mode is over-damped for a small portion of the glacial parameter space where conduit radii are small and conduit lengths are on the ice-sheet scale. Crack dip also plays an important role, by controlling the degree to which oscillatory flow in the conduit interacts with branching cracks. As shown in Fig. 8, the reflection coefficient increases with increasing dip angle. As the magnitude of the reflection coefficient tends to 1, more flow enters the crack to excite resonance. Figure 8B shows dip angle impacts higher frequency oscillations more than lower frequencies, but generally cracks with high dip angles will be more connected hydraulically with the conduit during fluid oscillation.

Applications to the field

These limitations notwithstanding, our study suggests that excitation of resonant modes in coupled conduit–crack networks may provide a tool to infer englacial geometries in a range of realistic conditions. Appropriate instrumentation of glacial conduits, whether natural or human-made, is often more challenging than the equivalent problem in industry due to the dynamic conditions experienced on glaciers. However, the ability to directly instrument the fluid, such as with high-frequency pressure sensors or cameras, makes the detection of fluid resonance possibly simpler than for the equivalent volcanic problem. Field applications of the model developed here likely require a case-by-case examination. We illustrate how this might be accomplished by examining two contrasting glacial settings, where high-frequency pressure time series inside a vertical borehole already exist.

As a first example, we consider the results of Gräff and others (2019), who conducted experiments in a drilled borehole on Rhonegletscher Glacier in the Swiss Alps. Although their passive observations are not identical to our numerical experiments forced by a surface pressure pulse, they would exhibit the same eigenmodes of the system that we model all else constant. At the drilling site, Rhonegletscher Glacier was 117 m thick and was penetrated by hot water drilling with a hole of radius 10 cm. Gräff and others (2019) noted both impulsive and a more sustained excitation of crack waves in their borehole, resulting in high-frequency pressure time series qualitatively similar to our numerical experiments. They recorded several distinct spectral peaks that were inferred to represent resonant crack wave modes of a basal water-filled crack.

We propose that the range of spectral peaks observed by Gräff and others (2019) can be interpreted according to the framework introduced here for a conduit and basal crack. According to this model, the lowest frequency mode observed by Gräff and others (2019) will be the coupled mode, with higher frequency peaks being associated with crack and organ pipe modes. The relative amplitude of these modes will vary with the excitation function, which was not well constrained but might include both stick slip at the glacier bed and surface forcing. We therefore focus primarily on interpreting the eigenmodes themselves.

Using Eqn (40) and ice properties shown in Table 1, we calculate the crack length to be ~ 4.4 m for a coupled mode to match the ~ 1 Hz lowest frequency in (Gräff and others, 2019, Fig. 4). Our modeled quality factor of ~ 60 does not match with that reported of ~ 1.5, but does if we artificially increase viscous dissipation in the conduit by ~ 1000. This discrepancy suggests that our model does not account for all sources of dissipation present in the natural system. The next highest mode at ~ 2.3 Hz is consistent with an open-closed organ pipe mode for a 107 m water column in the conduit (the water surface was ~ 10 below the ice surface), assuming sufficient uncertainty in the estimated tube wave speed due variable ice properties to account for slight discrepancies between calculated organ pipe frequencies and observations. The ~ 8 Hz mode is consistent with a harmonic of this mode. We interpret the ~ 4 Hz mode to be the fundamental mode of the crack, since it cannot be explained by an organ pipe mode. However, we are unable to identify subsequent crack wave modes. Similar to Gräff and others (2019) we use Fig. 7 from Lipovsky and Dunham (2015) to determine a crack length using our interpreted fundamental frequency of 4 Hz. We determine a crack length of 5.8 m, which is remarkably close to the length inferred independently from the fundamental mode. Note that we cannot use results shown in Fig. 2 without modeling non-fully developed flow in the crack to accurately determine quality factor contours. Crack opening is predicted to be ~ 1 mm by the crack wave mode, but is unresolved by the coupled mode (crack storativity is sensitive to crack length only as in Eqn (12)).

Our interpretation differs from Gräff and others (2019), who associate the lowest observed frequency in the power spectrum with the fundamental crack eigenmode. This predicts a 19.8 m basal crack length. These authors also argue that the 2.3 ± 0.22 Hz peak does not reflect tube wave resonance, because it was not measured by a nearby surface seismometer. We do not attempt to assess this here, but argue that the relative self-consistency offered by our model for the full range of spectral peaks observed by Gräff and others (2019), despite its simplicity, is interesting and potentially compelling. Our results are consistent with a borehole connected to a thin, 4–5 m long, subglacial crack. In addition, if we consider the sustained events to be similar to the continuous forcing example in Fig. 9, differences between spectral content of an impulsive versus continuous surface forcing are in qualitative agreement with variations in spectral peak amplitude. In particular, reduction in amplitude of an open-closed organ pipe mode for the longer forcing wavelengths present in a continuous source is consistent with a coincident increase in amplitude of the coupled mode.

This result provides a measure of confidence that our model can reasonably be applied in the alpine environment. Limited availability of high-frequency data from ice sheets precludes a direct assessment of our methods in thick ice. But we consider representative experiments on the Greenland ice sheet as a template for whether englacial features should be detectable in that environment. In 2014 and 2015, drilled boreholes in SE Greenland near Isunnguata Sermia outlet glacier penetrated ~ 700 m thick ice (Meierbachtol and others, 2018), and were instrumented with 4 Hz pressure sensors at the glacier bed. For the majority of their sampling period the conduit was filled with ~ 600 m of water. Assuming a conduit radius similar to the boreholes of 15 cm (Meierbachtol and others, 2013), if a coupled mode is excited, we could constrain a crack length up to ~ 70 m before the gravity-dominated regime limits inference of crack dimensions.

Although no resonant oscillations in the pressure time series were reported by Meierbachtol and others (2018), transient

pressure pulses with a duration of ∼ 10–20 s were reported. The signals qualitatively resemble over-damped waves and might be interpreted as such. Based on the geometry of the conduit, the coupled mode might not be over-damped if excited. Therefore, we consider the possibility of this over-damped pulse originating from the basal water layer, given that the pressure transducer was located at base of the borehole. Figure 7 from Lipovsky and Dunham (2015) predicts that a 100 m long crack with an opening of ∼ 1 mm would result in a 0.1 Hz over-damped oscillation. Table 1 from Meierbachtol and others (2018) shows most pressure pulse recovery times are around 10 s, which matches the predicted periods. We recognize that, in practice, over-damped signals alone are not likely to result in strong constraints on englacial or subglacial geometry. But their existence could be used to motivate future experiments.

These examples suggest that low-frequency eigenmodes represent a promising tool for inferring englacial geometry in ice-sheet settings as well as alpine glaciers. The predictive power of the coupled mode is maximized for measurements in short conduit lengths ($L < 100$ m) and conduit radii larger than 50 cm (in order to detect cracks up to ∼100 m in length). In a controlled active source setting, one can control conduit radius (through drilling) which could help in designing experiments. Either continuous or impulsive forcing will excite low-frequency modes, and modulated frequency sweeping of input forcing could be leveraged to seek signatures of matched resonance (Liang and others, 2017) or be otherwise tuned to detect cracks of different sizes.

It is also possible that excitation of resonant signals could be used to probe time-evolving englacial or subglacial geometry. For example, seasonal evolution of subglacial drainage pathways (Gimbert and others, 2016) or lake drainage (e.g. Bigelow and others, 2020) occur on timescales long enough that one would expect to see systematic changes in resonant periods and quality factors as subsurface geometry evolves. We leave further investigation of these possibilities to future study.

Concluding remarks

Englacial geometry is an elusive missing piece of the glacial hydrologic system. In this study, we have investigated the limits for which fluid resonance could be used to gain insight into englacial geometries, through the analysis of wave propagation in generic coupled conduit–crack networks. We presented an overview of expected modes in the englacial system and focused on resonant modes that may be sensitive to englacial geometry. We showed that although there are many modes excited in complex englacial water transport networks, a resonant mode originating from the coupled oscillation of fluid into and out of a branching crack is the fundamental mode of the system and provides information on crack and conduit geometry. Future extensions of the modeling framework presented here could include more systematic characterization of coupled conduit and crack eigenmodes, examining boundary layer flow in the crack, adaptations to curved and cross-sectionally varying conduits, consideration of anisotropic elastic media, and modeling of seismic radiation in the ice associated with fluid motions. However, even in its present state, we believe that applications of the framework presented here to seismic and borehole water pressure studies could provide new insights on englacial transport and the englacial to subglacial connection.

References

Aki K, Fehler M and Das S (1977) Source mechanism of volcanic tremor: fluid-driven crack models and their application to the 1963 Kilauea eruption. *Journal of Volcanology and Geothermal Research* **2**(3), 259–287. doi: 10.1016/0377-0273(77)90003-8.

Anandakrishnan S and Alley RB (1997) Tidal forcing of basal seismicity of ice stream C, West Antarctica, observed far inland. *Journal of Geophysical Research Solid Earth* **102**(B7), 15183–15196. doi: 10.1029/97JB01073.

Andrews LC, and 8 others (2018) Seasonal evolution of the subglacial hydrologic system modified by supraglacial lake drainage in western Greenland. *Journal of Geophysical Research Earth Surface* **123**(6), 1479–1496. doi: 10.1029/2017jf004585.

Badgeley JA, and 6 others (2017) An englacial hydrologic system of brine within a cold glacier: Blood Falls, McMurdo Dry Valleys, Antarctica. *Journal of Glaciology* **63**(239), 387–400. doi: 10.1017/jog.2017.16.

Banwell A, Hewitt I, Willis I and Arnold N (2016) Moulin density controls drainage development beneath the Greenland ice sheet. *Journal of Geophysical Research Earth Surface* **121**(12), 2248–2269. doi: 10.1002/2015JF003801.

Bartholomew I, and 5 others (2012) Short-term variability in Greenland ice sheet motion forced by time-varying meltwater drainage: implications for the relationship between subglacial drainage system behavior and ice velocity. *Journal of Geophysical Research Earth Surface* **117**(F3), F03002. doi: 10.1029/2011jf002220.

Bigelow DG, and 5 others (2020) The role of englacial hydrology in the filling and drainage of an ice-dammed lake, Kaskawulsh Glacier, Yukon, Canada. *Journal of Geophysical Research Earth Surface* **125**(2), e2019JF005110. doi: https://doi.org/10.1029/2019JF005110.

Biot MA (1952) Propagation of elastic waves in a cylindrical bore containing a fluid. *Journal of Applied Physics* **23**(9), 997–1005. doi: 10.1063/1.1702365.

Burridge R, Kostek S and Kurkjian AL (1993) Tube waves, seismic waves and effective sources. *Wave Motion* **18**(2), 163–210. doi: 10.11016/0165-2125(93)90046-i.

Catania GA, Neumann TA and Price SF (2008) Characterizing englacial drainage in the ablation zone of the Greenland ice sheet. *Journal of Glaciology* **54**(187), 567–578. doi: 10.3189/002214308786570854.

Chen X, Quan Y and Harris JM (1996) Seismogram synthesis for radially layered media using the generalized reflection/transmission coefficients method: theory and applications to acoustic logging. *Geophysics* **61**(4), 1150–1159. doi: 10.1190/1.1444035.

Chouet B (1988) Resonance of a fluid-driven crack: radiation properties and implications for the source of long-period events and harmonic tremor. *Journal of Geophysical Research* **93**(B5), 4375–4400. doi: https://doi.org/10.1029/JB093iB05p04375.

Chouet B and Dawson P (2013) Very long period conduit oscillations induced by rockfalls at Kilauea Volcano, Hawaii. *Journal of Geophysical Research Solid Earth* **118**, 5352–5371. doi: 10.1002/jgrb.50376.

Crouch SL, Starfield AM and Rizzo FJ (1983) Boundary element methods in solid mechanics. *Journal of Applied Mechanics* **50**(3), 704–705. doi: 10.1115/1.3167130.

Del Rey Fernández DC, Hicken JE and Zingg DW (2014) Review of summation-by-parts operators with simultaneous approximation terms for the numerical solution of partial differential equations. *Computers & Fluids* **95**, 171–196. doi: 10.1016/j.compfluid.2014.02.016.

Dunham EM and Ogden DE (2012) Guided waves along fluid-filled cracks in elastic solids and instability at high flow rates. *Journal of Applied Mechanics* **79**(3), 031020. doi: 10.1115/1.4005961.

Engelhardt H and Kamb B (1997) Basal hydraulic system of a west Antarctic ice stream: constraints from borehole observations. *Journal of Glaciology* **43**(144), 207–230. doi: 10.3189/s0022143000003166.

Erickson BA, O'Reilly O and Nordström J (2019) Accuracy of stable, high-order finite difference methods for hyperbolic systems with non-smooth wave speeds. *Journal of Scientific Computing* **81**(3), 2356–2387. doi: 10.1007/s10915-019-01088-w.

Ferrazzini V and Aki K (1987) Slow waves trapped in a fluid-filled infinite crack: implication for volcanic tremor. *Journal of Geophysical Research* **92**(B9), 9215. doi: 10.1029/jb092ib09p09215.

Fountain AG, Schlichting RB, Jansson P and Jacobel RW (2005) Observations of englacial water passages: a fracture-dominated system. *Annals of Glaciology* **40**, 25–30. doi: 10.3189/172756405781813762.

Gimbert F, Tsai VC, Amundson JM, Bartholomaus TC and Walter JI (2016) Subseasonal changes observed in subglacial channel pressure, size, and sediment transport. *Geophysical Research Letters* **43**, 3786–3794. doi: https://doi.org/10.1002/2016GL068337.

Gräff D, Walter F and Lipovsky BP (2019) Crack wave resonances within the basal water layer. *Annals of Glaciology* **60**(79), 158–166. doi: 10.1017/aog.2019.8.

Gulley J, Benn DI, Müuller D and Luckman A (2009) A cut-and-closure origin for englacial conduits in uncrevassed regions of polythermal glaciers. *Journal of Glaciology* **189**(55), 66–80. doi: https://doi.org/10.3189/002214309788608930.

Holzhausen G and Egan H (1986) Fracture diagnostics in east Texas and western Colorado using the hydraulic-impedance method. In *SPE Unconventional Gas Technology Symposium*, SPE-15215-MS, Society of Petroleum Engineers, Louisville, Kentucky (doi: 10.2118/15215-MS).

Iken A (1972) Measurements of water pressure in moulins as part of a movement study of the White Glacier, Axel Heiberg Island, Northwest Territories, Canada. *Journal of Glaciology* **11**(61), 53–58. doi: 10.3189/s0022143000022486.

Iken A, Fabri K and Funk M (1996) Water storage and subglacial drainage conditions inferred from borehole measurements on Gornergletscher, Valais, Switzerland. *Journal of Glaciology* **42**(141), 233–248. doi: 10.3189/s0022143000004093.

Karlstrom L and Dunham EM (2016) Excitation and resonance of acoustic-gravity waves in a column of stratified, bubbly magma. *Journal of Fluid Mechanics* **797**, 431–470. doi: 10.1017/jfm.2016.257.

Kavanaugh JL and Clarke GKC (2001) Abrupt glacier motion and reorganization of basal shear stress following the establishment of a connected drainage system. *Journal of Glaciology* **47**(158), 472–480. doi: 10.3189/172756501781831972.

Kavanaugh JL, Moore PL, Dow CF and Sanders JW (2010) Using pressure pulse seismology to examine basal criticality and the influence of sticky spots on glacial flow. *Journal of Geophysical Research* **115**(F4), F04025. doi: 10.1029/2010jf001666.

Krauklis P (1962) On some low-frequency vibrations of a liquid layer in an elastic medium. *Journal of Applied Mathematics and Mechanics* **26**(6), 1685–1692. doi: 10.1016/0021-8928(62)90203-4.

Kulessa B, Hubbard B, Williamson M and Brown GH (2005) Hydrogeological analysis of slug tests in glacier boreholes. *Journal of Glaciology* **51**(173), 269–280. doi: 10.3189/172756505781829458.

Liang C, Karlstrom L and Dunham EM (2020) Magma oscillations in a conduit-reservoir system, application to very long period (VLP) seismicity at basaltic volcanoes: 1. Theory. *Journal of Geophysical Research Solid Earth* **125**(1), e2019JB017437. doi: 10.1029/2019JB017437.

Liang C, O'Reilly O, Dunham EM and Moos D (2017) Hydraulic fracture diagnostics from Krauklis-wave resonance and tube-wave reflections. *Geophysics* **82**(3), D171–D186. doi: 10.1190/geo2016-0480.1.

Lighthill J (1978) *Waves in Fluids*. Cambridge, UK: Cambridge University Press.

Lipovsky BP and Dunham EM (2015) Vibrational modes of hydraulic fractures: inference of fracture geometry from resonant frequencies and attenuation. *Journal of Geophysical Research Solid Earth* **120**(2), 1080–1107. doi: 10.1002/2014JB011286.

Meierbachtol T, Harper J and Humphrey N (2013) Basal drainage system response to increasing surface melt on the Greenland ice sheet. *Science* **341**(6147), 777–779. doi: 10.1126/science.1235905.

Meierbachtol TW, Harper JT and Humphrey NF (2018) Short duration water pressure transients in western Greenland's subglacial drainage system. *Journal of Glaciology* **64**(64), 171–174. doi: 10.1017/jog.2018.9.

Mondal S (2010) *Pressure transients in wellbores: Water hammer effects and implications for fracture diagnostics*. Ph.D. thesis, The University of Texas at Austin.

Norris AN (1990) The speed of a tube wave. *The Journal of the Acoustical Society of America* **87**(1), 414–417. doi: 10.1121/1.399262.

Okada Y (1985) Surface deformation due to shear and tensile faults in a half-space. *Bulletin of the Seismological Society of America* **75**(4), 1135–1154.

O'Reilly O, Dunham EM and Nordström J (2017) Simulation of wave propagation along fluid-filled cracks using high-order summation-by-parts operators and implicit-explicit time stepping. *SIAM Journal on Scientific Computing* **39**(4), B675–B702. doi: 10.1137/16M1097511.

Petrenko VF and Whitworth RW (2002) *Physics of Ice*. Oxford, UK: Oxford University Press. doi: 10.1093/acprof:oso/9780198518945.001.0001.

Podolskiy EA (2020) Toward the acoustic detection of two-phase flow patterns and Helmholtz resonators in englacial drainage systems. *Geophysical Research Letters* **47**(6), e2020GL086951. doi: 10.1029/2020GL086951.

Prochnow B, O'Reilly O, Dunham EM and Petersson NA (2017) Treatment of the polar coordinate singularity in axisymmetric wave propagation using high-order summation-by-parts operators on a staggered grid. *Computers & Fluids* **149**, 138–149. doi: 10.1016/j.compfluid.2017.03.015.

Rada C and Schoof C (2018) Channelized, distributed, and disconnected: subglacial drainage under a valley glacier in the Yukon. *The Cryosphere* **12**(8), 2609–2636. doi: 10.5194/tc-12-2609-2018.

Roeoesli C, Walter F, Ampuero JP and Kissling E (2016) Seismic moulin tremor: seismic moulin tremor. *Journal of Geophysical Research Solid Earth* **121**(8), 5838–5858. doi: 10.1002/2015JB012786.

Röthlisberger H (1972) Water pressure in intra- and subglacial channels. *Journal of Glaciology* **11**(62), 177–203.

Schoof C (2010) Ice-sheet acceleration driven by melt supply variability. *Nature* **468**(7325), 803–806. doi: 10.1038/nature09618.

Segall P (2010) *Earthquake and Volcano Deformation*. Princeton, NJ, USA: Princeton University Press.

Sheriff RE and Geldart LP (1995) *Exploration seismology*, 2nd Edn.Cambridge, New York: Cambridge University Press.

Shreve RL (1972) Movement of water in glaciers. *Journal of Glaciology* **11**(62), 205–214.

Spring U and Hutter K (1982) Conduit flow of a fluid through its solid phase and its application to intraglacial channel flow. *International Journal of Engineering Science* **20**(2), 327–363. doi: https://doi.org/10.1016/0020-7225(82)90029-5.

Stone DB, Clarke GKC and Ellis RG (1997) Inversion of borehole-response test data for estimation of subglacial hydraulic properties. *Journal of Glaciology* **43**(143), 103–113. doi: 10.3189/s0022143000002860.

Tang XM and Cheng CH (1993) Borehole Stoneley wave propagation across permeable structures. *Geophysical Prospecting* **41**(2), 165–187. doi: 10.1111/j.1365-2478.1993.tb00864.x.

Tsai VC and Rice JR (2010) A model for turbulent hydraulic fracture and application to crack propagation at glacier beds. *Journal of Geophysical Research* **115**(F3). doi: 10.1029/2009jf001474.

Vatne G (2001) Geometry of englacial water conduits, Austre Brøggerbreen, Svalbard. *Norsk Geografisk Tidsskrift* **55**(2), 85–93. doi: 10.1080/00291950152105136.

West ME, Larsen CF, Truffer M, O'Neel S and LeBlanc L (2010) Glacier microseismicity. *Geology* **38**(4), 319–322. doi: 10.1130/G30606.1.

Womersley JR (1955) Method for the calculation of velocity, rate of flow and viscous drag in arteries when the pressure gradient is known. *The Journal of Physiology* **127**(3), 553–563. doi: 10.1113/jphysiol.1955.sp005276.